Nature Communications

https://doi.org/10.1038/s41467-026-70833-1

Article in Press

Plasmonic Dirac-vortex lasers via three-dimensional photonic mass vortices engineering

Received: 28 August 2025

Accepted: 6 March 2026

Cite this article as: Zhong, M., Bi, X., Song, M. *et al.* Plasmonic Dirac-vortex lasers via three-dimensional photonic mass vortices engineering. *Nat Commun* (2026). https://doi.org/10.1038/s41467-026-70833-1

Mou Zhong, Xiaoqiong Bi, Mengyuan Song, Nanli Mou, Delin Zhang, Xiaolu Zhuo, Jingtian Hu, Biye Xie, Xianyu Ao & Jun Guan

Plasmonic Dirac-vortex lasers via three-dimensional photonic mass vortices engineering

Mou Zhong[1], Xiaoqiong Bi[2], Mengyuan Song[2], Nanli Mou[1], Delin Zhang[1], Xiaolu Zhuo[1], Jingtian Hu[3,4], Biye Xie[1], Xianyu Ao[2] and Jun Guan[1]*

[1] School of Science and Engineering, The Chinese University of Hong Kong (Shenzhen), Shenzhen, Guangdong, 518172, P. R. China

[2] Shandong Provincial Key Laboratory of Light Field Manipulation Physics and Applications, & School of Physics and Optoelectronics, Shandong Normal University, Jinan, 250358, P. R. China

[3] Guangdong Provincial Key Laboratory of Semiconductor Optoelectronic Materials and Intelligent Photonic Systems, Harbin Institute of Technology, Shenzhen, 518055, P. R. China

[4] Quantum Science Center of Guangdong-Hong Kong-Macan Greater Bay Area, Shenzhen, 518055, P. R. China

*E-mail: guanjun@cuhk.edu.cn

ABSTRACT

Topological photonic crystals provide a powerful platform for manipulating light. However, their flexibility in realizing diverse far-field beam profiles and polarization states is limited by the number of spatial symmetries lattices can provide. Here, we demonstrate plasmonic Dirac-vortex lasers with controlled polarization and intensity distributions by engineering photonic mass vortices in a three-dimensional parameter space. We design plasmonic Dirac-vortex cavities consisting of honeycomb lattices of aluminum nanoparticles, where photonic mass vortices are achieved by arranging distorted unit cells in an angular winding configuration. By manipulating the radial and azimuthal displacements of the nanoparticles as well as their size, taken as the third dimension of the system, we predict far-field radiation with spatially programmable polarization states and asymmetric intensity distributions. Experimentally, this is achieved by integrating organic dye molecules within the plasmonic Dirac-vortex cavities. Our work establishes a paradigm for multi-dimensional mass-enabled cavity engineering, which offers flexibility in sculpting exotic photonic states with broad implications for photonic circuits, quantum devices, and bosonic systems.

INTRODUCTION

Manipulation of light properties, including amplitude, polarization, and phase, plays a key role in emerging technological applications[1], such as super-resolution imaging[2-5], free-space optical communications[6-8], holography[9,10], and quantum information processing[11-14]. To generate structured light with customizable field distributions, a variety of techniques, including liquid-crystal spatial light modulators[15], metasurfaces[11,16,17], and photonic integrated circuits[18,19], have been developed. However, these approaches typically demand stringent wavefront shaping, precise optical alignment, and rely on external illumination systems; these factors hinder the system scalability and integration capacity.

Topological photonics offer a platform to engineer radiation characteristics by directly leveraging photonic eigenmodes in micro- and nano-scale cavities[20-23]. Inspired by analogies to quantum spin Hall (QSH) effects[24,25], quantum valley Hall (QVH) effects[26], and bound states in the continuum (BICs)[27-29] in condensed matter physics, symmetry-engineered photonic lattices have enabled topologically protected eigenmodes capable of emitting nontrivial structured light[30-32]. Of particular interest is the concept of Dirac-vortex cavities[33-38], motivated by theoretical predictions of electron fractionalization in two-dimensional graphene with Dirac mass vortices[39-41]. These systems, described by a two-dimensional Dirac equation with a phase-winding mass term, support zero-dimensional eigenmodes that are topologically bound to the vortex core and robustly pinned at mid-gap frequency. Experimental implementations of Dirac-vortex photonic crystals have demonstrated lasing in the near-infrared[36,42] and mid-infrared[35,37] wavelengths, where the emission exhibits large free spectral ranges and nontrivial far-field beam profiles. Realizing Dirac-vortex cavities in the visible range has been challenging due to the limited availability of high-refractive-index materials and the stringent fabrication precision required at the nanoscale. Moreover,

current topological cavity designs face limitations in tailoring the complex properties of emitted light. The conventional Kekulé modulation schemes generate donut-shaped vector beams[35,37,42], and combinations of QSH and QVH photonic crystals produce linear polarized outputs[36]. The generation of structured light with arbitrarily designed polarization and intensity distributions has not been possible in topological cavities due to the limited modulation approaches.

Plasmonic nanostructures offer a promising platform for manipulating topological photonic phenomena. In contrast to high-refractive-index dielectric materials, plasmonic materials interact with light through collective oscillations of conduction electrons, which can enable strong light scattering and deep-subwavelength field confinement[43-45]. By exploiting the symmetry of plasmonic lattices, unidirectional QSH[46] and QVH[47] topological edge states have been demonstrated, and chiral mode responses have also been observed in plasmonic Kagome lattices[48]. Moreover, by precisely controlling the propagation and interference of surface plasmon polaritons, optical quasiparticles such as optical skyrmions have been constructed and detected[4,49-51]. Integrating plasmonic lattices with gain materials and introducing symmetry engineering such as BICs[52,53], chiral plasmonic lattice[54] and moiré lattice stacking[55,56] enables high-precision control over the topological charge and emission direction of vector beams, which broadens the toolbox for light engineering. However, multi-dimensional symmetry-breaking in plasmonic unit cells has not been explored, which restricts the realization of topological modes for complex laser emission characteristics.

Here we demonstrate plasmonic Dirac-vortex topological lasers that utilize three-dimensional (3D) photonic mass term design to modulate emission intensity distributions and polarization states. We showed that in honeycomb lattices of aluminum nanoparticles, distortions to the unit cells act as effective

photonic mass terms, which can lift the degeneracy of the double Dirac cone and introduce band inversion. To manipulate the photonic mass term, we constructed a 3D parameter space based on the radial displacement, azimuthal displacement, and nanoparticle size in unit cells. By arranging distorted unit cells in an angular winding configuration, we first designed a plasmonic Dirac-vortex cavity with C_3 symmetry, where the far-field radiation exhibits a vector beam with three lobes. By further tuning the particle sizes to break the inversion symmetry, we suppressed the intervalley coupling along selected directions and numerically demonstrated far-field beams with spatially varying polarizations and asymmetric intensity distributions. We integrated organic dye molecules with plasmonic Dirac-vortex cavities, and experimentally achieved single-mode lasing with vector-polarized donut-shaped emission. By systematically varying the mass vortex design scheme, we realized lasing beam patterns with diverse polarization textures, including vector beams, linearly polarized beams, and complex polarization states with non-uniform energy distributions.

RESULTS

Plasmonic Dirac-vortex lasers with 3D mass vortices

We design plasmonic Dirac-vortex cavities based on the coupling of localized surface plasmons of metal nanoparticles. The initial structure consists of aluminum nanoparticles arranged in a honeycomb lattice. Each nanoparticle in the lattice supports plasmonic dipole modes polarized in the *x*-*y* plane, which gives rise to evanescent electromagnetic fields at the metal surface. The coupling of nanoparticles in the lattice determines the photonic dispersion curve. Generally, the effective Hamiltonian of the wave system in each honeycomb unit cell can be expressed as

$$\boldsymbol{H}(k) = v_D\tau_0 \otimes \left(k_x\sigma_1 + k_y\sigma_2\right) + (\Delta_1\tau_1 - \Delta_2\tau_2 + \Delta_3\tau_3) \otimes \sigma_3 \quad (1)$$

where v_D is the Fermi velocity determining the slope of the Dirac cone, $\mathbf{k} = (k_x, k_y)$ is the in-plane wavevector, σ_i and τ_i are identical ($i = 0$) and Pauli matrices ($i = 1,2,3$) (Supplementary Note 1.1). Bandgaps emerge from the non-zero mass terms $\Delta_i (i = 1,2,3)$, which are induced by three independent parameters to change the translational symmetry and break the C_2 rotational symmetry that governs spatial inversion in the 2D lattice. When these components are combined into a 3D vector $\boldsymbol{\Delta} = (\Delta_1, \Delta_2, \Delta_3)$, the symmetry-breaking modulation of a series of unit cells can be described by

$$\boldsymbol{\Delta} = \Delta_0(\hat{\mathbf{u}} \cdot \cos(w \cdot \varphi) + \hat{\mathbf{v}} \cdot \sin(w \cdot \varphi)) \quad (2)$$

where $\hat{\mathbf{u}}$ and $\hat{\mathbf{v}}$ are three-component orthogonal unit vectors, φ is the modulation phase, and w is the winding number of mass vortices. To construct a Dirac-vortex cavity, we map the modulation phase φ onto real space, such that the cavity center is surrounded by unit cells exhibiting azimuthally graded photonic mass terms. Arranging these mass terms in a vortex configuration around a center modifies the boundary conditions of the cavity modes, and thus introduces an additional winding phase φ into the

eigenmodes of the system, which enables $|w|$ zero-dimensional topological defect states, known as the Dirac-vortex states[34,39,40,57].

We show that the plasmonic Dirac-vortex laser can be modulated by 3D photonic mass terms (**Figure 1**). At the center area of the cavity, aluminum nanoparticles are arranged in a honeycomb lattice. Surrounding this central region, a global modulation scheme (inset of **Figure 1**) is applied to the honeycomb lattice to construct a Dirac-vortex cavity (Supplementary Note 2). Spatially mapping the modulation phase φ into real space creates a non-zero mass vortex; this winding configuration provides a topological constraint that localizes an isolated zero-energy mode at the vortex core area. The far-field polarization is determined by the near-field spatial distribution of the Bloch-mode profile of the cavity mode, which is constrained by the vortex-induced boundary conditions. Symmetry-breaking in the 3D parameter space enables mass vortex modulation and thus can result in tailored far-field polarization and intensity profiles. By integrating organic dye molecules with the Dirac-vortex cavities, lasing emission can be achieved, where the polarization and intensity distributions are direct manifestations of the engineered topological properties.

Design of plasmonic Dirac-vortex cavities

We first show how the distortions to the unit cells of the aluminum honeycomb lattices can act as effective photonic mass terms and enable topological mode engineering. To obtain a cavity mode of coupled dipoles in the visible range, we choose the unit cell edge length of $a = 265$ nm, nanoparticle radius of $r = 53$ nm and height of $h = 65$ nm (**Figure 2a**). We define a 3D parameter space based on the radial displacement δ_k, azimuthal displacement δ_m and nanoparticle size δ_i, which can introduce non-zero effective photonic mass terms in the Hamiltonian of the system. We divide the metal

nanoparticles into two groups to preserve the C_3-rotation symmetry. The first group consists of particles with radius $r_1 = r + 0.35\delta_i$ and the second group consists of particles with radius $r_2 = r - 0.35\delta_i$; the coefficient 0.35 is chosen for an optimized bandgap width. The displacements δ_k and δ_m break the translational symmetry along the vector $\mathbf{P} = (\frac{\sqrt{3}a}{2}, \frac{a}{2})$ and a non-zero δ_i breaks the inversion symmetry of the lattice.

The 3D parameters within the unit cell represent three independent degrees of freedom in the lattice mass term $\mathbf{\Delta} = (\Delta_1, \Delta_2, \Delta_3)$, which can be collectively described by a three-component perturbation vector $\boldsymbol{\delta} = (\delta_k, \delta_m, \delta_i)$. We fix the magnitude of the perturbation vector to $|\boldsymbol{\delta}| = \delta_0 = 0.16a$ such that all possible $\boldsymbol{\delta}$ lie on the surface of a sphere in a 3D parameter space (**Figure 2b**). The parameter space directly governs lattice symmetry and photonic mass terms (Supplementary Note 3.1). Notably, δ_k approximately controls the contraction and expansion of nanoparticles within the unit cell, and δ_i controls the sizes of two distinct nanoparticle groups without altering translational symmetry; these two parameters correspond directly to the structural configurations enabling photonic analogs of the QSH and QVH effects, respectively.

We design a series of continuously varying non-zero geometry modulations described by

$$\boldsymbol{\delta} = \delta_0(\hat{\mathbf{u}}\cos(w \cdot \varphi) + \hat{\mathbf{n}} \times \hat{\mathbf{u}}\sin(w \cdot \varphi)) \tag{3}$$

where δ_0 is the magnitude of the perturbation vector, w is the winding number, φ is the modulation phase, $\hat{\mathbf{n}}$ is the unit vector normal to the perturbation parameter plane, and $\hat{\mathbf{u}}$ is the unit vector pointing to the starting point for the modulation. Here we set $w = 1$ to ensure the formation of an isolated topological mode. Each great circle on the parameter sphere corresponds to a set of mass vortex

configurations characterized by the orthogonal unit vectors ($\hat{\mathbf{n}}$ and $\hat{\mathbf{u}}$) and a modulation phase φ, which enables the construction of Dirac-vortex cavities.

We first consider the special case of $\hat{\mathbf{n}} = (0,0,1)$, where the distortion parameters are restricted to the δ_k-δ_m plane. Because the unit cells are enlarged to a group of three primitive cells in the honeycomb lattice, the Dirac cones at $\mathrm{K}_{\pm}$ points can be folded to the Γ point, which results in a double degenerate Dirac cone located inside the light cone (**Figure 2c**, gray curves). The geometry perturbations δ_k and δ_m affect the translational symmetry, which enables intervalley coupling between K_+ and K_- and opens a bandgap in the system (red dashed curves). Meanwhile, the C_3 rotational symmetry ensures frequency degeneracy of the two states at each band edge of the local bandgap at the Γ point, which is essential for maintaining the orbital and valley degrees of freedom required in various topological phenomena such as photonic QSH and QVH effects. Maintaining this C_3 symmetry thus provides a robust platform for realizing plasmonic Dirac-vortex states.

We show that both the bandgap size and the double degenerate Bloch modes at the Γ-point band edges vary with the modulation phase φ (**Figure 2d**). Crucially, any pair of unit cells with modulation phases differing by π exhibits opposite geometric distortions and inverted Bloch mode distributions between their upper and lower bands (Supplementary Note 3.2). For example, at $\varphi = 0$, the long-wavelength bands exhibit Bloch modes with d-like orbital character, while the short-wavelength bands exhibit p-like Bloch modes. As the modulation phase is increased by π, the mode profiles are exchanged, which indicates a band inversion. We note that the observed periodicity of $2\pi/3$ for the band gap size originates from the C_3-symmetric modulation of nanoparticle interaction strength, and the periodicity of π for the Bloch mode inversion results from the inversion of the mass term of the unit cell. By mapping

this azimuthal dependence to a real-space vortex profile, the non-trivial winding of the mass terms can produce a topologically protected zero-energy mode (Supplementary Note 1.2).

Figure 2e shows the complete design of the plasmonic Dirac-vortex cavity. We define the right nanoparticle of the center unit cell as the cavity center $\mathbf{r_0} = (\sqrt{3}a/3,0)$, which is also the core of mass vortices. Choosing this position as the center ensures that the complete Dirac-vortex cavity formed by this modulation scheme preserves C_3 symmetry[33]. Away from the center, we gradually introduce distortions to construct a spatially modulated aperiodic lattice. We define the magnitude of the perturbation using a hyperbolic tangent function

$$|\boldsymbol{\delta}(\mathbf{r})| = \delta_0 \tanh\left(\left|\frac{\mathbf{r}-\mathbf{r_0}}{R}\right|^4\right) \quad (4)$$

where R is the radius of the vortex core, which controls the mode volumes of the cavity modes. The choice of the hyperbolic tangent function can enable a potential well centered at the cavity with a smooth introduction of the mass term, which can reduce the optical loss of the cavity modes[33,36]. We establish the relation of the modulation phase and the azimuthal angle of the position vector using $\varphi(\mathbf{r}) = \arg(\mathbf{r})$. The mass vortex exhibits an angular distribution around the cavity center, which provides topological protection for the emergence of plasmonic Dirac-vortex states in the cavity via the Jackiw-Rossi mechanism[58]. We note that reducing the vortex radius *R* can decrease the mode volume but typically results in a lower quality factor of the cavity and a larger divergence angle in the far field. The winding number *w* determines the number of cavity modes and the topological charge of the far-field vector beam, which offers an additional parameter for light manipulation. In our design, we fixed $R = 3a$ and $w = 1$ for illustration.

Based on the 3D full wave electromagnetic simulation of the vortex lattice structure, an isolated mode is tightly bound in the center area of the cavity, which reveals the existence of a plasmonic Dirac-vortex state (**Figure 2e**). The simulation results present the spatial distribution of the electric field magnitude on the xy-plane located at the center of the nanoparticles, as well as on the vertical cross-sections in the yOz and xOz planes. The wavelength of the Dirac-vortex state is 600 nm, shorter than the wavelength of the Dirac point $(633$ nm$)$. This blueshift results from the finite cavity size and limited number of unperturbed lattice periods. When the size of the vortex core increases, the mode wavelength gradually approaches that of the Dirac point[33,35]. The peaks of $|\mathbf{E}|$ distribute around the central nanoparticle and gradually decay away from the cavity center along the xy-plane. Along the z-direction, the field decays evanescently, consistent with the behavior of plasmonic modes. The simulated field profile exhibits clear C_3 rotational symmetry in agreement with the structural symmetry of the cavity. Under the protection of the winding mass vortex, the Dirac-vortex state remains stably confined at the vortex core area and is robust against local defects or fabrication imperfections (Supplementary Note 4).

To analyze the far-field radiation of the Dirac-vortex state, we calculated the Rayleigh-Sommerfeld diffraction pattern of the near-fields. The resulting radiation pattern shows a vector polarized donut beam with three main intensity lobes (**Figure 2f**). We further analyzed the E_x (**Figure 2g**) and E_y (**Figure 2h**) polarized electromagnetic fields, whose superposition forms an azimuthally polarized vector beam carrying a topological charge of 1. The donut shape arises from the symmetry protection of the honeycomb lattice at the vortex core area, which prevents energy leakage through deconstruction interference. In contrast, the distorted unit cells change the translational symmetry, which enables coupling to radiative modes within the light cone and allows energy leakage into the continuum. The

angular variation in radiation intensities, which results from the position-dependent band structure across the cavity, further reflects the C_3 symmetry of the system. The Fourier transform of the near-field $|\mathbf{E}|$ distribution shows intensity maxima of equal magnitude at six $K_{\pm}$ points in the Brillouin zone before band folding (**Figure 2i**), which is a key signature of the topological nature of the mode originating from intervalley coupling. The non-zero intensity at the center of the Fourier transform image corresponds to the energy of the Dirac-vortex state coupled into the far field. We note that this cavity model is equivalent to the well-known Kekulé modulation[33,35,39-41], which represents a special case within our broader design framework.

Photonic mass vortex engineering in 3D parameter space

We further consider the breaking of inversion symmetry and introduce a generalized plasmonic Dirac-vortex design by modulating the third dimension of the perturbation vector δ_i. The modulation scheme is defined by the normal vector $\hat{\mathbf{n}} = (-1/2, 1/\sqrt{2}, 1/2)$ and vector $\hat{\mathbf{u}} = (-1/2, -1/\sqrt{2}, 1/2)$ (**Figure 3a**). The band gap size and Bloch mode evolve with the modulation phase φ, where band inversion occurs with a change of φ by π (**Figure 3b**). Unlike the distinctly localized Bloch mode in the *C*3-symmetric cavity (**Figure 2e**) where the $|\mathbf{E}|$ surrounds the rightmost nanoparticle per unit cell with *C*3 symmetry, the Bloch mode profiles after introducing an additional inversion symmetry breaking (**Figure 3c**) exhibits a different distribution with its maximum amplitude distributed over multiple adjacent nanoparticles. The 3D mass term modulation alters the far-field radiation pattern, which transforms the donut-shaped profile into an asymmetric intensity distribution (**Figure 3d**) with azimuthally varying polarization. This difference results from the introduction of δ_i for broken inversion symmetry, which weakens the effect from translational symmetry breaking. Consequently, the mass

vortex introduced by this 3D modulation scheme exhibits weaker intervalley coupling, which suppresses radiative emission along corresponding directions. The Fourier transform of the $|\mathbf{E}|$ distribution (**Figure 3e**) reveals the non-uniform energy distribution across the six $K_{\pm}$ points, which indicates weakened mode coupling between the K_{+} and K_{-} valleys. Furthermore, the direction-dependent intensity variations suggest that the strength of the intervalley coupling exhibits an anisotropic characteristic across the Dirac-vortex cavity.

Experimental realization of plasmonic Dirac-vortex lasers

To experimentally verify the existence of plasmonic Dirac-vortex modes, we fabricated a Dirac-vortex cavity composed of aluminum nanoparticles on a quartz substrate (Methods and Supplementary Note 2). Due to the relatively high Ohmic loss of metal nanoparticles, the simulated quality factor of the cavity is limited to ~80, which makes direct optical characterization challenging. To overcome this, we introduced optical gain and an optical waveguide by putting approximately $0.6\ \mu L$ of a dimethyl sulfoxide (DMSO) solution containing Rhodamine 6G (R6G) dye onto the nanoparticle cavity and sealed the liquid with a quartz coverslip (**Figure 4a**). Surface tension and negative pressure between the two quartz surfaces result in a stable structure, which forms an approximately $1\ \mu m$ thick gain layer. The DMSO (refractive index ~1.48[59]) and quartz (refractive index ~1.46[60]) together form a planar waveguide structure, and the hybridization between plasmonic and waveguide modes can result in hybrid waveguide-plasmonic modes[61-63] (Supplementary Note 5.1).

The morphology of the fabricated Dirac-vortex cavities was characterized by capturing the optical and scanning electron microscope (SEM) images (**Figure 4b**, **Figure 4c** and Supplementary Note 6). We optically pumped the Dirac-vortex laser devices using a 532 nm, 0.7 ns pulsed laser, and collected the

emission spectra as a function of pump energy density (**Figure 4d** and Supplementary Note 7). With increased pump intensities, the spontaneous emission was enhanced, and a lasing threshold was observed at a pump energy density of $4.3\ \mathrm{mJ/cm^2}$, above which a narrowband lasing peak emerged at 581 nm. We note that this lasing wavelength does not correspond to the surface plasmon resonance mode but rather aligns with the Γ-point of the hexagonal lattice diffraction band structure. This is because the energy distributions are dominated by waveguide modes, and the plasmonic lattice determines the topological character and optical feedback (Supplementary Note 5.2). Despite the distinct electromagnetic field distributions of the plasmonic modes and waveguide-plasmonic modes, both acquire equivalent photonic mass terms due to identical symmetry-breaking mechanisms. The laser operates in a stable single longitudinal mode with a side-mode suppression ratio (SMSR) exceeding 50 dB. The mode purity is attributed to the topological protection of the cavity, where an isolated state protected by a photonic mass vortex robustly operates at the Dirac point. At the lasing threshold, we observed a distinct spectral narrowing, with the full width at half maximum (FWHM) reduced to approximately $0.14\ \mathrm{nm}$ (**Figure 4e**), close to the spectrometer resolution limit of $0.12\ \mathrm{nm}$. A slight broadening of the linewidth appeared at higher pump energies, which results from the thermal accumulation effects within the cavity.

The angle-resolved photoluminescence (PL) spectra below threshold (**Figure 4f**) reveal fluorescence enhancement at the Γ-point of the lattice. The measured dispersion curve is close to the calculated dispersion based on the empty lattice approximation of hybrid waveguide-plasmonic modes. We note that the spectral features observed in **Figure 4f** do not correspond to the pure plasmonic modes. Due to the low Q-factor and strong Ohmic loss, plasmonic resonances cannot support lasing under our experimental conditions. Instead, the measured dispersions of enhanced PL arise from hybrid waveguide-plasmonic

modes, where the periodic aluminum nanoparticle lattice acts as a weak perturbation, which results in a band structure that closely matches the empty lattice approximation (Supplementary Note 5.1). The far-field laser emission pattern, imaged at the back focal plane (**Figure 4g**), exhibits a donut-like intensity distribution with azimuthal vector polarization. This characteristic distribution aligns with the expected features of a transverse electric (TE)-polarized Dirac-vortex cavity (**Figures 2f-h**), indicating that the metallic nanoparticles introduce a critical modulation to the electromagnetic fields and facilitate the formation of the Dirac-vortex state, from which the laser emission originates. We note that although both TE-polarized and transverse magnetic (TM)-polarized cavity modes theoretically exist, in our experiment, the in-plane polarized pump laser sources facilitate stronger in-plane polarized emission from the dye molecules, which results in a tendency to excite the TE-polarized Dirac-vortex cavity modes. Moreover, the plasmonic nanoparticles exhibit a larger in-plane polarizability due to their larger transverse dimensions, which further enhances the excitation of in-plane polarized TE-like cavity modes. We showed that the plasmonic Dirac-vortex laser exhibits a small divergence angle of approximately 1° (Supplementary Note 8), because the introduction of the waveguide can reduce the photonic bandgap and thus increase the mode volume of the cavity mode for a directional laser output (Supplementary Note 5).

Programmable far-field laser emission characteristics

Building upon the realization of a plasmonic Dirac-vortex laser, we further investigate whether diverse Dirac-vortex cavity designs, enabled by tuning the mass vortices design scheme, can universally support topological state lasing, and how these designs affect the optical characteristics of the structured light emission. Five Dirac-vortex cavity design schemes are illustrated, each corresponding to a different mass vortex in 3D parameter space (first row of **Figure 5**). We show that all five designs enabled stable

single-mode lasing (second row of **Figures 5**), which indicates the robustness of the plasmonic Dirac-vortex state across a wide range of modulation configurations. The simulated and measured far-field radiation patterns (third row of **Figures 5** and fourth row of **Figure 5**, respectively) further reveal how the symmetry and polarization of the emission evolve with the modulation scheme (Supplementary Note 9).

In **Figures 5a**, we keep the normal vector $\hat{\mathbf{n}} = (0, 0, 1)$, which is the same as the design scheme in **Figure 2b**, and varied the in-plane starting vector from $\hat{\mathbf{u}} = (1, 0, 0)$ to $\hat{\mathbf{u}} = (0, -1, 0)$. **Figure 5k** and **Figure 5p** illustrate the calculated and measured far-field patterns, respectively. Both simulations and experiments demonstrate that for the Dirac-vortex cavities, keeping the vector $\hat{\mathbf{n}}$ unchanged, the far-field intensity distribution maintains the shape but rotates by 90° as the initial vector $\hat{\mathbf{u}}$ varies by 90°. Meanwhile, the polarization state changes from an azimuthally polarized vector beam to a cylindrical vector beam characterized by a fixed angular deviation of 45° between the local polarization vector and the radial direction at every spatial position, thereby forming a spatially chiral polarization texture. These results indicate that rotating the initial vector of the mass vortex is not equivalent to physically rotating the cavity. Instead, the change of the geometry symmetry alters the intricate interference of electromagnetic waves within the lattice, leading to the rotation of the far-field pattern and the transformation of the polarization distribution (Supplementary Note 10). **Figure 5b** and **Figure 5c** illustrate mass vortex designs formed by combining δ_i with δ_k or δ_m. The far-field patterns show that introducing δ_i transforms the donut-shaped profile into a symmetric intensity pattern with two main lobes. This enables the generation of fully 45° linearly polarized (**Figure 5q**) or horizontally linearly polarized (**Figure 5r**) beams.

We further demonstrate the generality of our design scheme using arbitrary mass vortex configurations in 3D parameter space (**Figure 5d** and **Figure 5e**). Any great circle on the parameter sphere corresponds to a mass vortex of a specific plasmonic Dirac-vortex state. Under these designs, the optical field intensity is no longer uniform, which allows a strong main lobe to emerge at an arbitrary azimuthal position. The polarization can exhibit vector character (**Figure 5s**) or be designed as linear (**Figure 5t**). By computing the topological charge of the far-field pattern, we showed that under Kekulé modulation, a polarization vortex with a well-defined topological singularity appears at the far-field center; in contrast, introducing δ_i progressively shifts the singularity away and destroys the linear azimuthal dependence of the polarization angle (Supplementary Note 11). These results indicate that our 3D mass-vortex design enables not only the tailoring of far-field intensity and polarization distributions, but also precise control over the phase landscape of the far-field polarization vortex. Our work establishes a general design framework where mass-term engineering allows flexible shaping of the far-field emission beams in plasmonic Dirac-vortex lasers. Unlike previous works limited to 1D or 2D parameter spaces[23,33,36], our strategy integrates multiple symmetry-breaking into a single cavity platform, which enables plasmonic Dirac-vortex laser emission with complex polarization states and non-uniform intensity distributions. We note that the low output efficiency of the plasmonic Dirac-vortex lasers (~ 0.1%) could potentially be improved by a combination of efficient gain media and optimized cavity designs (Supplementary Note 7). In addition, the strong field confinement of plasmonic modes can also enable rich photonic spin textures, which, combined with mass vortices engineering in Dirac-vortex states, provide a platform for constructing diverse quasiparticles (Supplementary Note 12).

DISCUSSION

In conclusion, we have demonstrated plasmonic Dirac-vortex lasers operating in the visible wavelengths with programmable polarization and intensity profiles based on 3D mass vortices engineering. By mapping the unit cell distortion from a 3D parameter sphere onto real space, we showed plasmonic topological states protected by non-trivial winding mass vortices with engineered near-field and far-field distributions, going beyond the scope of classical Kekulé modulation schemes. Experimentally, we achieved lasing with a wide range of emission patterns, including vector beams, linearly polarized beams, and structured beams with spatially varying polarization and intensity. Our approach simultaneously breaks translational and inversion symmetries, which enables design schemes distinct from conventional QSH or QVH topological degrees of freedom and provides a general framework for exploring spin textures physics, non-Hermitian physics, and nonlinear optics. Furthermore, our design paradigm enables flexible and deterministic control over optical field configurations in topological microcavities, which offers a promising platform for robust structured light sources in applications such as free-space optical communication, holography, super-resolution imaging, and quantum photonics.

METHODS

Numerical simulation

The band structure and modes within the unit cells were calculated using 3D simulations in COMSOL Multiphysics. Periodic boundary conditions were implemented on the six boundaries of the honeycomb lattice to simulate infinite lattices. Perfectly matched layer (PML) boundary conditions were applied at z direction to truncate the simulation domain effectively. The optical constants of Al were adopted from the

experimental data reported by Cheng et al. (2016)[64]. For the analysis of plasmonic modes, Al nanoparticles were positioned at the center with background refractive index of 1.46. In the case of hybrid waveguide-plasmonic modes, Al nanoparticles were positioned on quartz (n ~1.46[60]) substrate and immersed in 1-μm-thick DMSO solution (n ~1.48[59]). Above the DMSO, a quartz cover glass was positioned, and a PML boundary condition was applied at the top of the simulation domain. The eigenmodes and their frequencies of Dirac-vortex states were calculated by additional simulations in COMSOL Multiphysics. A perfect magnetic conductor (PMC) boundary condition was established at the plane $z = 0$. An Al nanoparticle cavity with a height of 32.5 nm was set above the PMC boundary. The nanoparticles were surrounded by a 400-nm-thick layer of DMSO solution. A PML layer was applied to the top region of the simulation domain, and the cavity was enclosed by scattering boundary conditions. Data visualizations were generated using the perceptually uniform color maps in the ColorCET library[65,66].

Fabrication

A standard procedure for fabricating aluminum nanoparticle arrays via lift-off processing was implemented as follows. First, a cleaned quartz substrate was spin-coated with a 150-nm-thick layer of polymethyl methacrylate (PMMA) photoresist. To enhance conductivity during electron-beam lithography (EBL), a 60-nm-thick conductive polymer layer (Electra) was subsequently applied. The designed pattern was then transferred to the PMMA layer using EBL. After exposure, any residual conductive polymer was thoroughly rinsed with deionized water, followed by development of the exposed resist. Subsequently, any remaining residues were removed using inductively coupled plasma treatment. A 65-nm-thick aluminum nanoparticle layer was deposited via electron-beam evaporation. To finalize the

fabrication, the remaining photoresist was lifted off by immersing the sample in N-Methyl-2-pyrrolidone (NMP) at 70 °C.

Optical measurement

The sample was mounted on a translational stage and optically pumped at room temperature by a pulsed 532 nm laser (repetition rate: 200 Hz; pulse width: 0.7 ns), which was focused through a lens onto the center of the Dirac-vortex cavity, forming a circular excitation spot approximately 200 μm in diameter. The emitted light was collected from the opposite side of the sample using a $10\times$, 0.3 NA objective lens and directed to real-space imaging, momentum-space (k-space) imaging, and angle-resolved spectral analysis (Supplementary Not 7).

DATA AVAILABILITY

The data generated during this study have been deposited in the Zenodo repository[67]: https://doi.org/10.5281/zenodo.18700663.

REFERENCES

1 Forbes, A., De Oliveira, M. & Dennis, M. R. Structured light. *Nat. Photonics* **15**, 253-262 (2021).

2 Hell, S. W. Far-field optical nanoscopy. *Science* **316**, 1153-1158 (2007).

3 Pancaldi, M. *et al.* High-resolution ptychographic imaging at a seeded free-electron laser source using OAM beams. *Optica* **11**, 403-411 (2024). https://doi.org/10.1364/OPTICA.509745

4 Du, L., Yang, A., Zayats, A. V. & Yuan, X. Deep-subwavelength features of photonic skyrmions in a confined electromagnetic field with orbital angular momentum. *Nat. Phys.* **15**, 650-654 (2019). https://doi.org/10.1038/s41567-019-0487-7

5 Ji, Z. *et al.* Multidimensional multiplexing metalens for STED microscopy. *Sci. Adv.* **11**, eadt2807 (2025). https://doi.org/doi:10.1126/sciadv.adt2807

6 Morita, R. *et al.* High-speed high-power free-space optical communication via directly modulated watt-class photonic-crystal surface-emitting lasers. *Optica* **11**, 971-979 (2024). https://doi.org/10.1364/OPTICA.523421

7 Inoue, T. *et al.* Frequency-modulated high-power photonic-crystal surface-emitting lasers for long-distance coherent free-space optical communications. *Nat. Photonics* **19**, 1330-1335 (2025). https://doi.org/10.1038/s41566-025-01782-2

8 Mou, N. L. *et al.* Gradient moiré perovskite superlattices for laser beam steering. *Science Advances* **11** (2025). https://doi.org/10.1126/sciadv.adz8028

9 Dorrah, A. H. *et al.* Light sheets for continuous-depth holography and three-dimensional volumetric displays. *Nat. Photonics* **17**, 427-434 (2023). https://doi.org/10.1038/s41566-023-01188-y

10 Gao, X. *et al.* Discontinuous orbital angular momentum metasurface holography. *Nat. Commun.* **16**, 10688 (2025). https://doi.org/10.1038/s41467-025-65722-y

11 Jia, W. *et al.* Polarization-entangled Bell state generation from an epsilon-near-zero metasurface. *Sci. Adv.* **11**, eads3576 (2025). https://doi.org/10.1126/sciadv.ads3576

12 Mirhosseini, M. *et al.* High-dimensional quantum cryptography with twisted light. *New Journal of Physics* **17**, 033033 (2015).

13 Ornelas, P., Nape, I., de Mello Koch, R. & Forbes, A. Non-local skyrmions as topologically resilient quantum entangled states of light. *Nat. Photonics* **18**, 258-266 (2024). https://doi.org/10.1038/s41566-023-01360-4

14 Li, L. *et al.* Metalens-array–based high-dimensional and multiphoton quantum source. *Science* **368**, 1487-1490 (2020). https://doi.org/10.1126/science.aba9779

15 Zheng, Z.-g. *et al.* Three-dimensional control of the helical axis of a chiral nematic liquid crystal by light. *Nature* **531**, 352-356 (2016).

16 Sroor, H. *et al.* High-purity orbital angular momentum states from a visible metasurface laser. *Nat. Photonics* **14**, 498-503 (2020). https://doi.org/10.1038/s41566-020-0623-z

17 Mou, N. L. *et al.* Large-Area Perovskite Nanocrystal Metasurfaces for Direction-Tunable Lasing. *Nano Letters* **24**, 12676-12683 (2024). https://doi.org/10.1021/acs.nanolett.4c03921

18 Bütow, J., Eismann, J. S., Sharma, V., Brandmüller, D. & Banzer, P. Generating free-space structured light with programmable integrated photonics. *Nat. Photonics* **18**, 243-249 (2024).

19 Pires, D. G., Rocha, J. C. A., Jesus-Silva, A. J. & Fonseca, E. J. S. Optical mode conversion through nonlinear two-wave mixing. *Phys. Rev. A* **100**, 043819 (2019). https://doi.org/10.1103/PhysRevA.100.043819

20 Hasan, M. Z. & Kane, C. L. Colloquium: Topological insulators. *Rev. Mod. Phys.* **82**, 3045-3067 (2010). https://doi.org/10.1103/RevModPhys.82.3045

21 Qi, X. L. & Zhang, S. C. Topological insulators and superconductors. *Rev. Mod. Phys.* **83** (2011). https://doi.org/10.1103/RevModPhys.83.1057

22 Fu, L. Topological Crystalline Insulators. *Phys. Rev. Lett.* **106**, 106802 (2011). https://doi.org/10.1103/PhysRevLett.106.106802

23 Chen, K. *et al.* Photonic Dirac cavities with spatially varying mass term. *Sci. Adv.* **9**, eabq4243 (2023). https://doi.org/10.1126/sciadv.abq4243

24 König, M. *et al.* Quantum Spin Hall Insulator State in HgTe Quantum Wells. *Science* **318**, 766-770 (2007). https://doi.org/doi:10.1126/science.1148047

25 Roth, A. *et al.* Nonlocal Transport in the Quantum Spin Hall State. *Science* **325**, 294-297 (2009). https://doi.org/doi:10.1126/science.1174736

26 Rycerz, A., Tworzydło, J. & Beenakker, C. W. J. Valley filter and valley valve in graphene. *Nat. Phys.* **3**, 172-175 (2007). https://doi.org/10.1038/nphys547

27 Wang, B. *et al.* Generating optical vortex beams by momentum-space polarization vortices centred at bound states in the continuum. *Nat. Photonics* **14**, 623-628 (2020). https://doi.org/10.1038/s41566-020-0658-1

28 Hsu, C. W., Zhen, B., Stone, A. D., Joannopoulos, J. D. & Soljačić, M. Bound states in the continuum. *Nat. Rev. Mater.* **1**, 16048 (2016). https://doi.org/10.1038/natrevmats.2016.48

29 Zeng, Y. *et al.* Metalasers with arbitrarily shaped wavefront. *Nature* **643**, 1240-1245 (2025). https://doi.org/10.1038/s41586-025-09275-6

30 Lu, L., Joannopoulos, J. D. & Soljačić, M. Topological photonics. *Nat. Photonics* **8**, 821-829 (2014). https://doi.org/10.1038/nphoton.2014.248

31 Ozawa, T. *et al.* Topological photonics. *Rev. Mod. Phys.* **91**, 015006 (2019). https://doi.org/10.1103/revmodphys.91.015006

32 Wang, Z., Chong, Y., Joannopoulos, J. D. & Soljačić, M. Observation of unidirectional backscattering-immune topological electromagnetic states. *Nature* **461**, 772-775 (2009). https://doi.org/10.1038/nature08293

33 Gao, X. *et al.* Dirac-vortex topological cavities. *Nat. Nanotechnol.* **15**, 1012-1018 (2020). https://doi.org/10.1038/s41565-020-0773-7

34 Ma, J., Xi, X., Li, Y. & Sun, X. Nanomechanical topological insulators with an auxiliary orbital degree of freedom. *Nat. Nanotechnol.* **16**, 576-583 (2021). https://doi.org/10.1038/s41565-021-00868-6

35 Han, S. *et al.* Photonic Majorana quantum cascade laser with polarization-winding emission. *Nat. Commun.* **14**, 707 (2023). https://doi.org/10.1038/s41467-023-36418-y

36 Ma, J. *et al.* Room-temperature continuous-wave topological Dirac-vortex microcavity lasers on silicon. *Light: Science & Applications* **12**, 255 (2023). https://doi.org/10.1038/s41377-023-01290-4

37 Liu, J. *et al.* High-power electrically pumped terahertz topological laser based on a surface metallic Dirac-vortex cavity. *Nat. Commun.* **15**, 4431 (2024). https://doi.org/10.1038/s41467-024-48788-y

38 Yan, B. *et al.* Topological Dirac-vortex modes in a three-dimensional photonic topological insulator. *Nat. Commun.* **16**, 5659 (2025). https://doi.org/10.1038/s41467-025-61238-7

39 Hou, C.-Y., Chamon, C. & Mudry, C. Electron fractionalization in two-dimensional graphenelike structures. *Phys. Rev. Lett.* **98**, 186809 (2007).

40 Iadecola, T., Schuster, T. & Chamon, C. Non-Abelian braiding of light. *Phys. Rev. Lett.* **117**, 073901 (2016).

41 Noh, J. *et al.* Braiding photonic topological zero modes. *Nat. Phys.* **16**, 989-993 (2020).

42 Yang, L., Li, G., Gao, X. & Lu, L. Topological-cavity surface-emitting laser. *Nat. Photonics* **16**, 279-283 (2022). https://doi.org/10.1038/s41566-022-00972-6

43 Guan, J. *et al.* Light–Matter Interactions in Hybrid Material Metasurfaces. *Chem. Rev.* **122**, 15177-15203 (2022). https://doi.org/10.1021/acs.chemrev.2c00011

44 Wang, W. *et al.* The rich photonic world of plasmonic nanoparticle arrays. *Materials Today* **21**, 303-314 (2018). https://doi.org/https://doi.org/10.1016/j.mattod.2017.09.002

45 Guan, J. *et al.* Plasmonic Nanoparticle Lattice Devices for White-Light Lasing. *Adv Mater* **35**, e2103262 (2023). https://doi.org/10.1002/adma.202103262

46 Honari-Latifpour, M. & Yousefi, L. Topological plasmonic edge states in a planar array of metallic nanoparticles. *Nanophotonics* **8**, 799-806 (2019). https://doi.org/doi:10.1515/nanoph-2018-0230

47 Wu, X. *et al.* Direct observation of valley-polarized topological edge states in designer surface plasmon crystals. *Nat. Commun.* **8**, 1304 (2017). https://doi.org/10.1038/s41467-017-01515-2

48 Juarez, X. G. *et al.* Chiral optical properties of plasmonic kagome lattices. *ACS Photonics* **11**, 673-681 (2024).

49 Tsesses, S. *et al.* Optical skyrmion lattice in evanescent electromagnetic fields. *Science* **361**, 993-996 (2018). https://doi.org/10.1126/science.aau0227

50 Shen, Y. *et al.* Optical skyrmions and other topological quasiparticles of light. *Nat. Photonics* **18**, 15-25 (2024). https://doi.org/10.1038/s41566-023-01325-7

51 Schwab, J. *et al.* Skyrmion bags of light in plasmonic moiré superlattices. *Nat. Phys.* **21**, 988–994 (2025).

https://doi.org/10.1038/s41567-025-02873-1

52 de Gaay Fortman, N. *et al.* Spontaneous symmetry breaking in plasmon lattice lasers. *Sci. Adv.* **10**, eadn2723 (2024). https://doi.org/10.1126/sciadv.adn2723

53 Song, M., Gao, X., Bai, C., Guan, J. & Ao, X. High-Quality Plasmonic Lasing with Topologically Trivial or Nontrivial Polarization. *ACS Photonics* **12**, 2252-2259 (2025). https://doi.org/10.1021/acsphotonics.5c00421

54 Hong, C., Zheng, Z., Patel, S. K. & Odom, T. W. High-Chirality Polariton Lasing from Symmetry-Broken Plasmonic Lattices. *ACS Nano* **19**, 18824-18832 (2025). https://doi.org/10.1021/acsnano.5c04290

55 Tan, M. J., Freire-Fernández, F. & Odom, T. W. Symmetry-Guided Engineering of Polarization by 2D Moire´ Metasurfaces. *ACS nano* **18**, 23181-23188 (2024).

56 Guan, J. *et al.* Far-field coupling between moiré photonic lattices. *Nat. Nanotechnol.* **18**, 514-520 (2023). https://doi.org/10.1038/s41565-023-01320-7

57 Jackiw, R. & Rossi, P. Zero modes of the vortex-fermion system. *Nucl. Phys. B* **190**, 681-691 (1981).

58 Wu, X. *et al.* Topological Corner Modes Induced by Dirac Vortices in Arbitrary Geometry. *Phys. Rev. Lett.* **126**, 226802 (2021). https://doi.org/10.1103/PhysRevLett.126.226802

59 Kozma, I. Z., Krok, P. & Riedle, E. Direct measurement of the group-velocity mismatch and derivation of the refractive-index dispersion for a variety of solvents in the ultraviolet. *J. Opt. Soc. Am. B* **22**, 1479-1485 (2005). https://doi.org/10.1364/JOSAB.22.001479

60 Arosa, Y. & de la Fuente, R. Refractive index spectroscopy and material dispersion in fused silica glass. *Opt. Lett.* **45**, 4268-4271 (2020). https://doi.org/10.1364/OL.395510

61 Schokker, A. H., van Riggelen, F., Hadad, Y., Alù, A. & Koenderink, A. F. Systematic study of the hybrid plasmonic-photonic band structure underlying lasing action of diffractive plasmon particle lattices. *Physical Review B* **95**, 085409 (2017). https://doi.org/10.1103/PhysRevB.95.085409

62 Guan, J. *et al.* Quantum Dot-Plasmon Lasing with Controlled Polarization Patterns. *ACS Nano* **14**, 3426-3433 (2020). https://doi.org/10.1021/acsnano.9b09466

63 Guan, J. *et al.* Engineering Directionality in Quantum Dot Shell Lasing Using Plasmonic Lattices. *Nano Letters* **20**, 1468-1474 (2020). https://doi.org/10.1021/acs.nanolett.9b05342

64 Cheng, F. *et al.* Epitaxial Growth of Atomically Smooth Aluminum on Silicon and Its Intrinsic Optical Properties. *ACS Nano* **10**, 9852-9860 (2016). https://doi.org/10.1021/acsnano.6b05556

65 Kovesi, P. Good colour maps: How to design them. *arXiv preprint arXiv:1509.03700* (2015).

66 Kovesi, P. Colorcet: Perceptually uniform colour maps. http://colorcet.com. (2020)

67 Zhong, M. Plasmonic Dirac-vortex lasers via three-dimensional photonic mass vortices engineering - source data. Zenodo. https://doi.org/10.5281/zenodo.18700663. (2026).

ACKNOWLEDGMENTS

This work was supported by National Natural Science Foundation of China (No. 12404442 to J.G., No. 12374310 to X. A., Nos. 62475225 and 12404187 to B.X., and No. 62405076 to J.H.), 1+1+1 CUHK-CUHK(SZ)-GDSTC Joint Collaboration Fund (No. 2025A0505000052 to J.G.), Shenzhen Science and

Technology Program (Nos. JCYJ20250604141202003, JCYJ20240813113603005, and RCBS20231211090623036 to J.G., No. JCYJ20240813104929039 to J.H., and JCYJ20240813113619025 to B.X.), Guangdong Basic and Applied Basic Research Foundation (No. 2023A1515110685 to J.G., No. 2025A1515011713 to J.H., and No. 2024A1515012031 to B.X.), Guangdong Basic Research Center of Excellence for Aggregate Science (to J.G.), Guangdong Provincial Key Laboratory of Semiconductor Optoelectronic Materials and Intelligent Photonic Systems (No. 2023B1212010003 to J.G. and J.H.), China Postdoctoral Science Foundation (No. 2024M753105 to N.M.), Guangdong Provincial Quantum Science Strategic Initiative (No. GDZX2506001 to J.G., and No. GDZX2306002 to J.H.), National Key R&D Program of China (No. 2023YFA1407700 to B.X.), Department of Science and Technology of Guangdong Province (Nos. 2023A1515110091 and 2023QN10C200 to X.Z.).

AUTHOR CONTRIBUTIONS

M.Z. and J.G. conceived the idea. M.Z. performed the simulations, designed the devices, and conducted the sample characterization and optical measurements. X.B. and M.S. fabricated the samples. N.M. and D.Z. assisted in data interpretation. B.X., J.H. and X.Z. contributed to refining the theoretical work. X.A. guided the sample fabrication. J.G. guided the experimental and theoretical investigations. M.Z. and J.G. wrote the manuscript, and all authors revised the manuscript.

Corresponding author

Correspondence to Jun Guan.

COMPETING INTERESTS

The authors declare no conflict of interest.

FIGURES

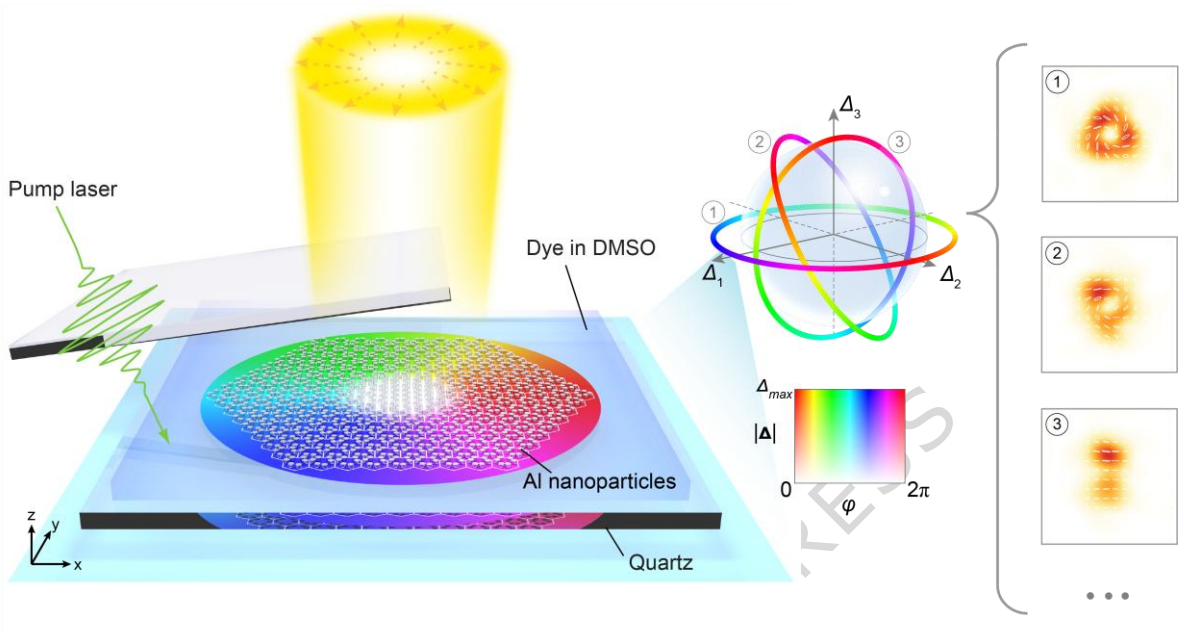

Figure 1. Plasmonic Dirac-vortex lasers with 3D mass vortices engineering. Scheme showing aluminum nanoparticles arranged in a honeycomb lattice with position-dependent photonic mass terms. The modulation phase is mapped onto real space, as indicated by the color scheme in the inset. The aluminum nanoparticle lattice is covered with a dye-dimethyl sulfoxide (DMSO) solution and a quartz coverslip. The mass vortices determined by $\boldsymbol{\Delta}$ enable optical Dirac-vortex cavity modes, which support lasing emission with engineered polarization and intensity profiles. Mass vortex 1, based on changes of two translational symmetries, enables the emission of donut-shaped vector beams. Mass vortex 2 combines three degrees of freedom, which allows asymmetric beam emission and unusual polarization properties. Mass vortex 3 incorporates a change in inversion symmetry along with one translational symmetry change, which results in linearly polarized beam emission.

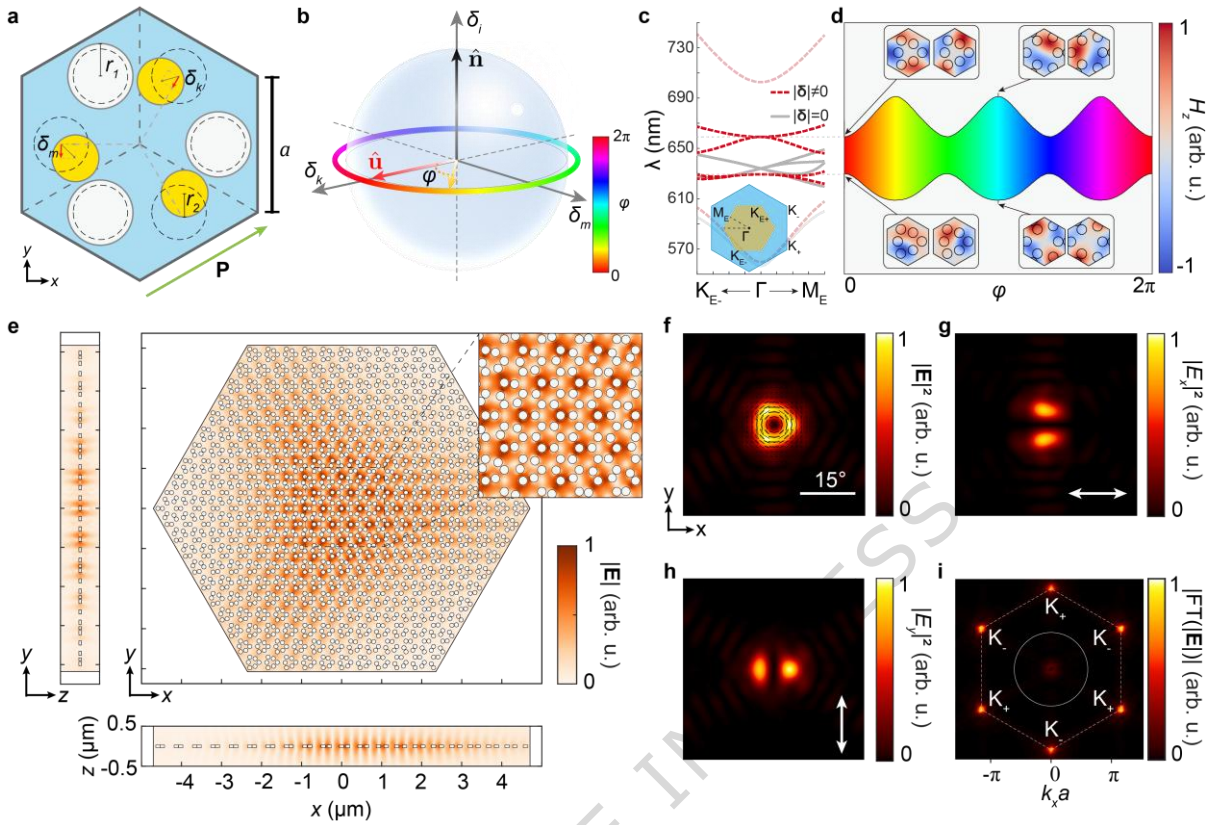

Figure 2. Design of plasmonic Dirac-vortex cavities. a Illustration of the detailed structure in a plasmonic lattice unit cell. The edge length of the unit cell is $a = 265$ nm. The radius of the white nanoparticles is $r_1 = 53\text{ nm} + 0.35\delta_i$, and the radius of the yellow nanoparticles is $r_2 = 53\text{ nm} - 0.35\delta_i$, with radial (δ_k) and azimuthal (δ_m) displacements. The dashed circles indicate the original particle positions and sizes. **b** Designed mass vortex in 3D parameter space. The parameter vector $\boldsymbol{\delta} = (\delta_k, \delta_m, \delta_i)$ introduces a non-zero 3D mass term. With fixed magnitude $\delta_0 = 0.16a$, the parameter $\boldsymbol{\delta}$ forms a mass term sphere. $\hat{\mathbf{n}} = (0,0,1)$ is the normal vector of the chosen parameter plane, and $\hat{\mathbf{u}} = (1,0,0)$ is the initial vector of the mass vortex. **c** Calculated band structure of a honeycomb plasmonic lattice. The undistorted case (gray curves) exhibits a double Dirac cone, and a bandgap opens at $\varphi = 0$ (red dashed curves) with distortions. The semi-transparent red lines refer to other bands of bulk states that do not participate in the zero-energy mode. Bottom inset: the first Brillouin zone of the unit cell, where the high-symmetry points at the edges (K_E and M_E) are indicated. **d** Calculated bandgap size and Bloch modes with the change of modulation phase φ. The insets depict H_z distributions of coupled plasmonic modes captured at 70-nm above the center of the nanoparticles, which exhibit double degeneracy. **e** Simulated near-field electric field magnitude $|\mathbf{E}|$ of the plasmonic Dirac-vortex state, taken through the center of the nanoparticles, which shows field confinement at the vortex core of the cavity. **f-h** Calculated far-field radiation pattern of the Dirac-vortex state, which shows a three-lobe vector vortex beam with radial polarization. The black lines refer to the polarization distributions. The white arrows refer to the *x* and *y* polarization components. **i** Magnitude of Fourier spectrum of the near-field $|\mathbf{E}|$, showing energy concentrated at six $K_\pm$ points of the unfolded unit cell (connected by white hexagon). The white circle indicates the light cone.

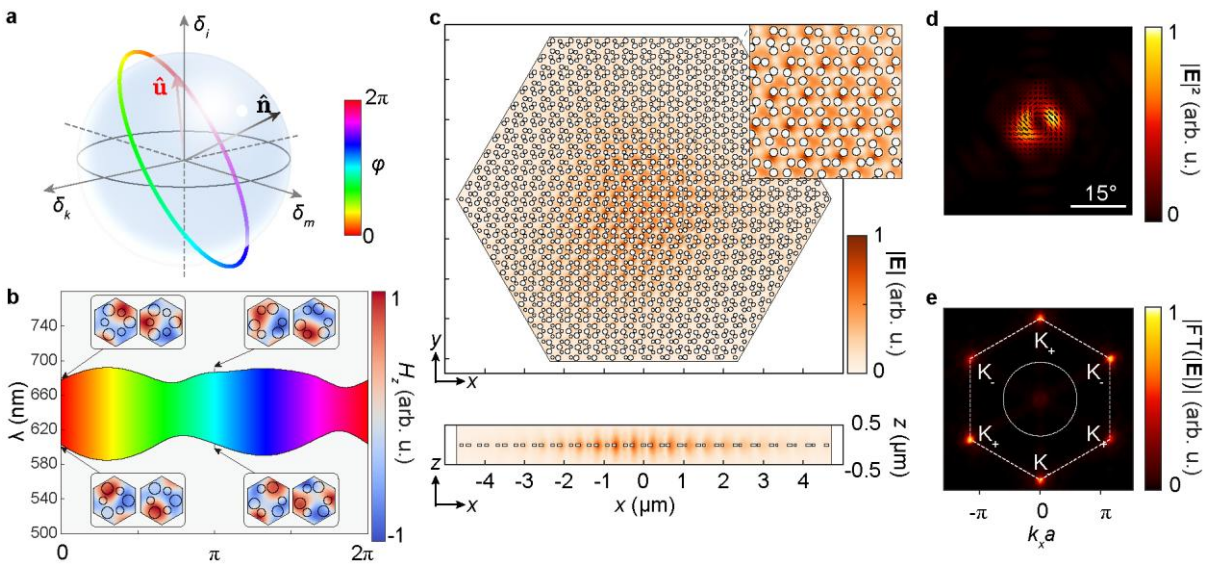

Figure 3. Photonic mass vortex engineering in 3D parameter space. a Scheme showing a mass vortex with $\hat{\mathbf{n}} = (-1/2, 1/\sqrt{2}, 1/2)$ and $\hat{\mathbf{u}} = (-1/2, -1/\sqrt{2}, 1/2)$. **b** Photonic bandgap size as a function of modulation phase φ, with double degenerate modes at band edges. **c** Simulated $|\mathbf{E}|$ of the near-fields. The field envelope is bound to the vortex core area, and the mass term in the third dimension induces distinct Bloch modes within the unit cell. **d** Calculated far-field pattern of the Dirac-vortex state. Black lines denote the polarization states of the far-field beam, which reveals a complex energy distribution and structured polarization profile. **e** Fourier spectrum of the near-field $|\mathbf{E}|$ component showing asymmetric energy concentration at six $K_{\pm}$ points (connected by white dashed lines). The white circle indicates the light cone.

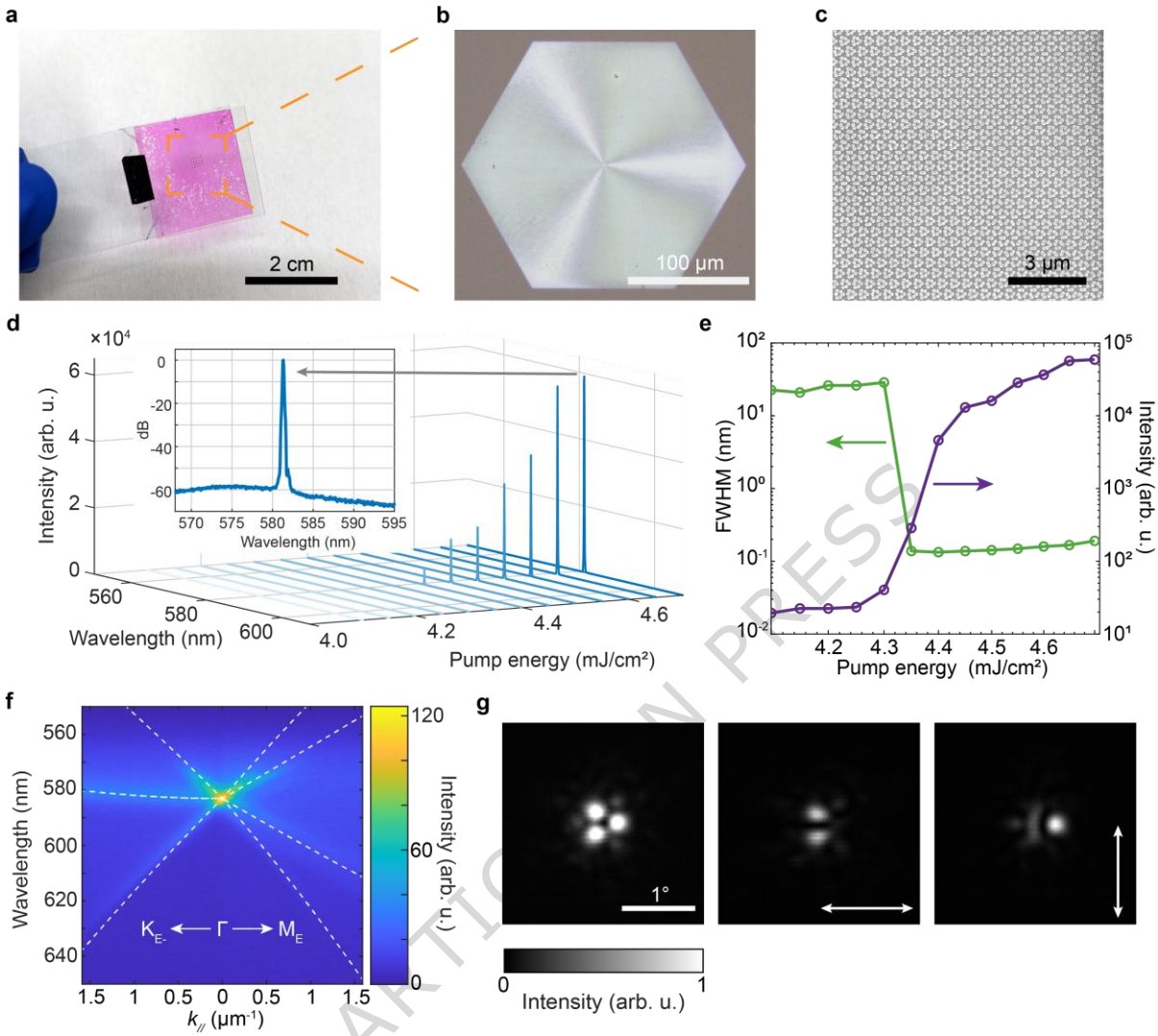

Figure 4. Experimental realization of plasmonic Dirac-vortex lasers. a Photo of Dirac-vortex lasers. The plasmonic Dirac-vortex cavities are immersed in DMSO solution with Rhodamine 6G (R6G) fluorescent dyes (pink) and sandwiched by two quartz substrates. **b** Optical microscope image of the Dirac-vortex cavity. **c** Scanning electron microscope image of the Dirac-vortex cavity with parameters $R = 3a$ and $\delta_0 = 0.16a$. **d** Experimentally measured emission spectra of the Dirac-vortex laser with the change of pump energy density. The inset shows a single-mode spectrum with a side-mode suppression ratio (SMSR) exceeding 50 dB. **e** Experimentally measured input-output curve and linewidths. **f** Measured angle-resolved photoluminescence spectra. White dashed lines denote the calculated photonic band structure based on the empty lattice approximation. **g** Experimentally measured far-field beam profiles. The white arrows indicate the polarization directions of the linear polarizer in front of the detector.

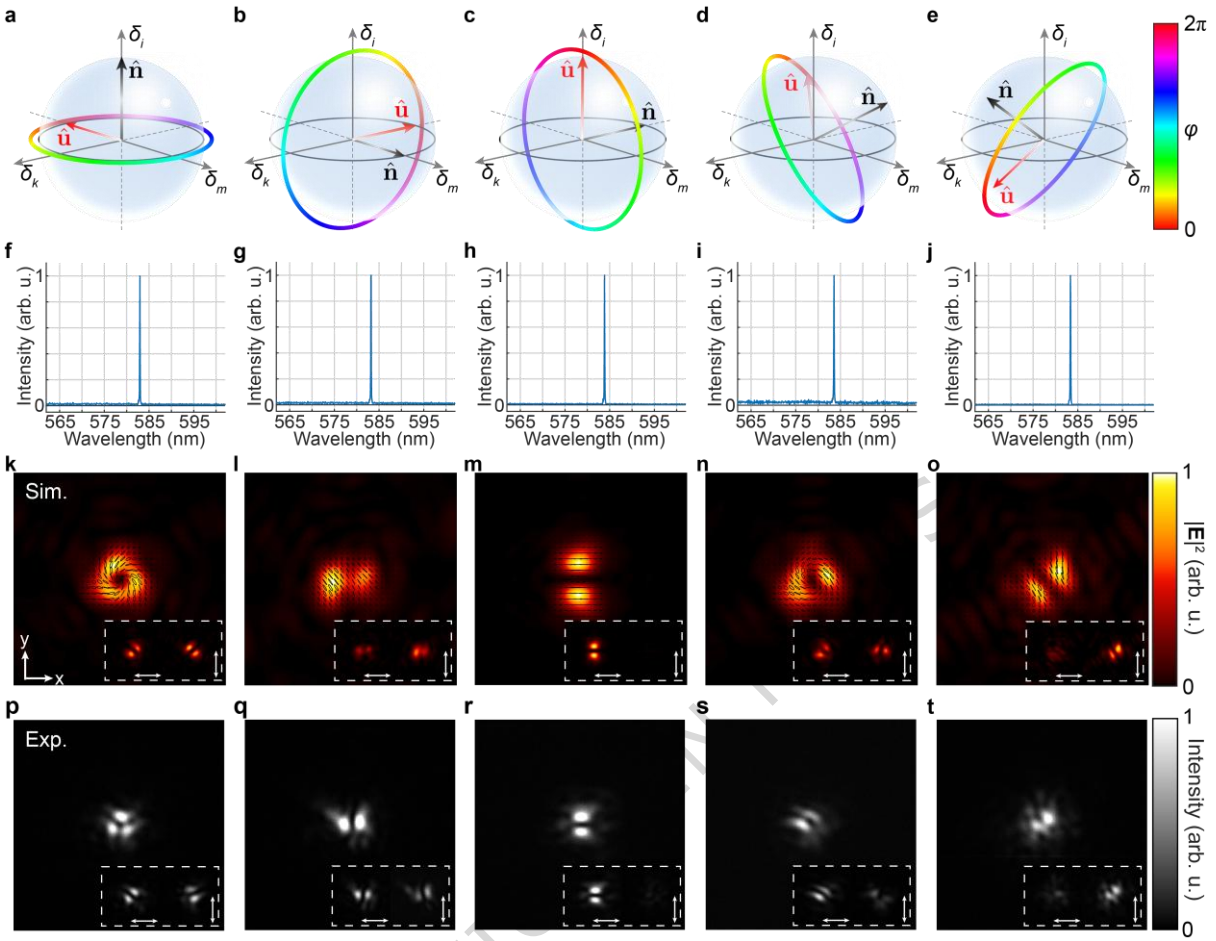

Figure 5. Complex laser emission characteristics with 3D photonic mass vortices engineering. a-e Schemes of mass term designs to manipulate beam profiles. **a-c** illustrate the Dirac-vortex cavities designed using any two of the three mass terms. **d-e** illustrate arbitrary mass vortex configurations in 3D parameter space. **f-j** Measured laser spectra corresponding to designs in (a-e). All devices operate in a single mode, with laser linewidths of <0.2 nm. **k-o** Simulated far-field patterns, and **p-t** measured far-field patterns corresponding to designs in (a-e).

SUPPLEMENTARY INFORMATION

Supplementary Information is provided as a separate file.